GPS Solut (2005) 9: 144–155
DOI 10.1007/s10291-005-0142-x

ORIGINAL ARTICLE

Georg Bergeton Larsen
Stig Syndergaard
Per Høeg
Martin Bjært Sørensen

Single frequency processing of Ørsted GPS radio occultation measurements

Received: 23 December 2004
Accepted: 5 February 2005
Published online: 21 May 2005

G. B. Larsen (✉) · M. B. Sørensen
Danish Meteorological Institute,
Lyngbyvej 100, DK-2100 Copenhagen,
Denmark
E-mail: gbl@dmi.dk
Tel.: +45-39-157489
Fax: +45-39-157460

S. Syndergaard
Institute of Atmospheric Physics,
The University of Arizona,
P.O. Box 210081, Tucson, AZ, 85721-0081

P. Høeg
Aalborg University, Niels Jernes Vej 14,
DK-9220 Aalborg, Denmark

Present address: S. Syndergaard
COSMIC Project Office,
University Corporation for Atmospheric
Research, P.O. Box 3000, Boulder, CO,
80307-3000

Abstract The Global Positioning System (GPS) radio occultation measurements obtained using the TurboRogue GPS receiver on the Danish satellite Ørsted have been processed using the single frequency method. Atmospheric profiles of refractivity and temperature are derived and validated against numerical weather prediction data from the European Centre for Medium-Range Weather Forecast (ECMWF). Results from the Ørsted GPS measurement campaign in February 2000 indicate that the single frequency method can provide retrievals with accuracy comparable to that of using two frequencies. From comparisons between measured dry temperature profiles and corresponding dry temperature profiles derived from ECMWF analysis fields, we find a mean difference of less than 0.5 K and a standard deviation of 2–4 K between 500 and 30 hPa in height. Above 30 hPa the impact of the ionosphere becomes more dominant and more difficult to eliminate using the single frequency method, and the results show degraded accuracy when compared to previous analysis results of occultation data from other missions using the dual frequency method. At latitudes less than 40° (denoted low latitudes), the standard deviation is generally smaller than at latitudes higher than 40° (denoted high latitudes). A small temperature bias is observed centered at 200 hPa for low latitudes and at 300 hPa for high latitudes. This indicates that the ECMWF analyses do not adequately resolve the tropopause temperature minimum. In the lowest part of the troposphere an observed warm bias is thought to be due to erroneous tracking of the GPS signal in cases of atmospheric multipath propagation.

Keywords GPS · Radio occultation · Remote sensing · Atmosphere

Introduction

The radio occultation technique exploiting the Global Positioning System (GPS) signals to monitor the Earth's atmosphere is a new method of remote sensing providing accurate profiles of atmospheric parameters with a great potential for Numerical Weather Prediction (NWP), climate monitoring, and atmosphere research studies. The radio occultation technique was originally developed for measurements of planetary atmospheres in the exploration of the solar system (e.g. Kliore et al. 1965; Fjeldbo et al. 1971). The implementation of the GPS in the late 1980's provided the necessary transmitting satellite constellation to make accurate retrieval of terrestrial atmospheric parameters feasible using the radio occultation technique (Yunck et al. 1988). In 1995 this

concept was proven by the successful GPS/MET experiment onboard the Microlab-1 satellite. The measurements by GPS/MET from April 1995 to 1997 showed that the technique is capable of retrieving profiles of, e.g., temperatures with a mean accuracy of less than 1 K between 1 and 40 km altitude and a standard deviation of 2–3 K (Rocken et al. 1997). Detailed descriptions of the processing of the GPS/MET data can be found in a number of publications (e.g. Schreiner et al. 1998; Hajj et al. 2002). Following the GPS/MET, the Danish satellite Ørsted was the second satellite capable of providing GPS radio occultation measurements. The Ørsted satellite with the primary goal to measure the Earth magnetic field was launched in February 1999, and in April 1999 the first radio occultation measurements were obtained. Since then a number of other GPS radio occultation missions have been launched. The most successful and productive among these are the German (Challenging Minisatellite Payload) CHAMP satellite (Wickert et al. 2004). In this paper we will describe the Ørsted GPS data processing of the neutral atmosphere with focus on the single frequency processing technique necessary for the Ørsted GPS occultations and present the results from the Ørsted measurement campaign with 19 days of continuous measurements in February 2000.

Data processing

The Ørsted GPS occultation data are collected by a TurboRogue receiver (Meehan et al. 1992; Thomas 1995) in a near-polar low earth orbit (LEO) at 650–830 km altitude (elliptical orbit). Additionally, a Trimble Advanced Navigation Sensor (TANS) GPS receiver collects data for orbit determination. The data from the Ørsted satellite are down-linked during each satellite pass over Copenhagen, approximately every five hours. The GPS data stream consists of the following data types: 1) Position and velocity fixes at 10 s intervals, which are the result of the GPS receivers crude onboard calculation based on all available GPS signals. These data are used as input to the calculation of the so-called initial orbits of the Ørsted satellite. 2) Low-rate data consisting of phase and pseudo-range measurements every 10 s. These data are used when more precise orbits are calculated using the initial orbits as input. 3) High-rate data consisting of phase measurements with a 10 Hz sampling rate, and Coarse Acquisition (CA) pseudo-range measurements with a 1 Hz sampling rate. The high-rate data are automatically acquired when GPS satellites descend through the last ~100 km of the atmosphere as seen from the Ørsted receiver. Nominally L_1 and L_2 phases are obtained from the raw data. However, for the Ørsted measurements the L_2 phase (as well as pseudo-range) data are erroneous due to a very low signal-to-noise ratio (SNR) and we need instead to perform ionosphere correction using the single frequency method (Montenbruck 2003).

Orbit determination

Ørsted initial orbits are calculated on the basis of position and velocity fixes from the down-linked data and the Earth orientation parameters using the GIPSY/OASIS software developed by the Jet Propulsion Laboratory (JPL) (Webb and Zumberge 1997). The International GPS Service (IGS), formed by the International Association of Geodesy (IAG), collect, archives, and distributes GPS observations from a large number of permanent tracking stations all over the world. On the basis of the initial orbits and phase and range observations from Ørsted and of the GPS orbits obtained from IGS, clock errors are estimated. The GPS orbits are used in the orbit determination for Ørsted and interpolated to a higher resolution for use in the retrieval of the atmospheric parameters.

Due to the erroneous L_2 phase and pseudo-range data, Ørsted final orbits have an uncertainty of about 50 mm/s in the velocity. This is generally not adequate for accurate retrieval of atmospheric parameters in the stratosphere. The problem is mitigated via a bias correction of retrieved bending angle profiles which is discussed in more detail later.

Excess phase

The data available for retrieval of atmospheric parameters are the L_1 phase measurements at 10 Hz sampling rate and the CA pseudo-range measurements (C_1) sampled at 1 Hz. Usually a combination of the L_1 and L_2 data is formed to eliminate the ionospheric effects. Using only single frequency measurements, a linear combination of the L_1 and C_1 data can be used to construct a quasi- L_2 phase (L_2*), but with the penalty of much more noise originating from the C_1 range. The resulting noise level on the constructed L_2* is several tens of cm with a temporal resolution of about 1 second. On top of this degradation, the Ørsted data is contaminated with data gaps of 1–2 second duration about every ten second due to an unfortunate interference with the activity of the satellite attitude control system.

Both these problems are solved in the data processing by a special filtering approach. The L_1 minus C_1 data are filtered with a low-pass filter and at the same time interpolated to 10 Hz (including patching the data gaps) using a regularization method minimizing second derivatives (Twomey 1977). The filter can be described as a matrix, F, given by

$$\mathbf{F} = (\tilde{\mathbf{I}} + \gamma \mathbf{S}^{\mathrm{T}}\mathbf{S})^{-1}, \quad (1)$$

where $\tilde{\mathbf{I}}$ is a "patchy" identity matrix, consisting of ones in the diagonal, but only for entries corresponding to where both L_1 and C_1 data are availably. Thus, with the desire to interpolate to 10 Hz, $\tilde{\mathbf{I}}$ is of approximate size 500×500, but with only about 50 elements in the diagonal being equal to one. Otherwise $\tilde{\mathbf{I}}$ consist of zeros. The matrix S is a second derivative, finite differences operator (see e.g. Twomey 1977, p. 125), S^T is its transpose, and γ is a regularization parameter determining the smoothing strength. We used $\gamma = 10^6$, corresponding to a low pass filter with a cut-off frequency of ~0.05 Hz. This cut-off frequency was chosen to effectively filter out the high frequency noise originating from the uncertainty in the C_1 data. The filtered (denoted by a bar) L_1 minus C_1 data is thus given by

$$\overline{\mathbf{L_1} - \mathbf{C_1}} = \mathbf{F}(\mathbf{L_1} - \mathbf{C_1}), \quad (2)$$

where (L_1-C_1) is a vector with about 500 elements, but with zeros at places where either L_1 or C_1 data are not available. The L_2* phase path is created from the L_1 phase observation and the filtered L_1 minus C_1 data as

$$L_2^* = L_1 - 0.5\left(1 - \frac{f_1^2}{f_2^2}\right)(\overline{L_1 - C_1}) \quad (3)$$

Principally an ionosphere-free combination, L_C, could be formed directly from the L_1 and C_1 signals (de la Torre Juàres et al. 2002), but creating a synthetic L_2* allows the further processing to be carried out in a standard way. Because of the low pass filter applied to the L_1 minus C_1 data, the high frequency (larger than ~0.05 Hz) ionospheric signal in L_1 is thus transmitted to L_2*, and will not be eliminated in the "ionosphere-free" combination. Although this is unfortunate, it is a compromise which has to be made in single-frequency processing of GPS occultation data, because accurate information about the high-frequency ionospheric signal is lost due to the very high level of noise and poor temporal resolution of the C_1 data.

Cycle slips occur because of temporary loss of lock in the signal tracking. During processing of Ørsted occultations, single cycle slips (either in Ørsted C_1 data or in ground-station L_C data) were detected and corrected in about 10% of the datasets based on the derivative of the data. Cycle slip detection and correction of the 10 Hz L_1 data was not attempted, but these data were quality-controlled based on the SNR. The TurboRogue receiver was designed to stop tracking after four seconds of low SNR, indicating that the signal has been occulted by Earth (Kursinski, personal communication, 2000). Not all occultations are tracked all the way to the surface, though. Often tracking is lost at a higher altitude for unknown reasons, and the last four seconds of data might still be useful. We therefore implemented an automated approach repeatedly cutting off 1 s of data in the last part of the phase time series if the L_1 SNR (averaged over the last 10 samples) was less than 55.

Clock errors originating from the GPS receiver onboard Ørsted and the transmitters onboard the GPS satellites are removed by using a double differencing technique, involving two GPS transmitters and a ground-station receiver with a stable external clock reference. The high-rate measurements from a net of ground-stations from various agencies (Fig. 1) are collected at 1 Hz sampling. From the beginning of year 2000 the amount of daily data downloaded at JPL was as high as ~250 megabytes. The coverage of ground-station data for the occultation events was greater than 98%.

The double differencing technique is illustrated in Figure 2. The GPS orbits and the ground station "orbits" are shifted/interpolated to the correct times of data transmission and reception, taking into account the signal travel-time. The time-shift is estimated from the measured C_1 and P_1 pseudo-ranges. Although the raw pseudo-ranges are subject to similar clock errors and relativistic frequency shifts as the phase paths, they are accurate enough for the purpose of estimating the signal travel time-shifts which are of order ~0.1 s for the GPS orbits and ~0.01 s for the ground stations. Similarly, the

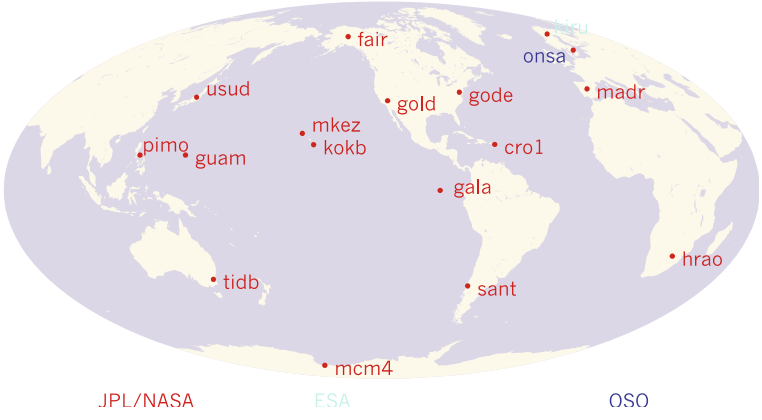

Fig. 1 Geographical distribution of the high-rate ground stations available during the February 2000 Ørsted campaign

ground-station LC phase data are also interpolated to the correct reception times. In the following we describe the double differencing in more details.

Usually the phase is expressed in terms of the phase path, i.e., the observed phase times the wavelength, c/f, where c is the speed of light in vacuum and f is the carrier frequency. The observed L_1 phase path can be written as a sum of different terms. In an earth-centered inertial (ECI) reference frame we write the observed L_1 phase path related to the occultation link (AB) as

$$L_{1AB} = \int_B^A n_1 ds_1 + Q_A - Q_B - \int \left(\frac{v_A^2}{2c} - \frac{\Phi_A}{c}\right) dt + \int \left(\frac{v_B^2}{2c} - \frac{\Phi_B}{c}\right) dt + \beta_{AB} + \varepsilon_{AB}. \quad (4)$$

In (4), the first integral is the desired L_1 phase path being the measure of the integration of the refractive index, n_1, along the occultation link between the transmitter and the receiver. The effect of oscillator generated clock errors in the receiver and the transmitter are symbolized by Q_A and Q_B, respectively. In addition to the oscillator generated clock errors there are also special and general relativistic clock shifts (Spilker 1980). In terms of accumulated shift in the observed phase path these are given by the two integrals over time as the occultation proceeds. The speeds of the satellites are denoted v_A and v_B, whereas Φ_A and Φ_B symbolizes the gravitational potentials at the heights of the satellites. Finally β_{AB} is the phase ambiguity term being a constant during the occultation, and ε_{AB} represents random thermal noise.

Only primary relativistic Doppler effects are included in (4). A secondary relativistic effect arises because the phase observations are collected, not in the ECI frame, but in the frame where the receiver is at rest. Thus the time-tags refer to the time in the receiver frame. Knowing the velocity and gravitational potential of the receiver, the time-tags could be transformed to the ECI frame, but the corresponding correction on the phase observations is of order v/c smaller than the relativistic terms already included in (4). Time-tag errors due to general and special relativity are therefore ignored.

It is worth noticing that a secondary general relativistic effect, known as the Shapiro effect (Shapiro 1964; Ashby 2003), does have a non-negligible effect on the observed phase path (a few cm), but it is almost constant during an occultation and the associated Doppler shift is only about 0.02 mm/s. Compared to the velocity errors of precise orbits for the Microlab-1 satellite which was estimated to be about 0.3 mm/s (Schreiner et al 1998), this is still small, and the Shapiro effect can be ignored unless more precise orbits can be obtained.

Because we are ultimately interested in the phase change during an occultation, in the following we disregard the phase ambiguity term, and for simplicity, also the random noise term. Given the velocities and the positions of the satellites and the ground station in the ECI reference frame, the relativistic terms can be modeled and subtracted. In the double differencing scheme, however, they cancel out as will be shown below. The clock error terms and the relativistic terms can be treated alike, and we therefore lump them into terms Ω_A and Ω_B for the receiver and the transmitter, respectively. With these simplifications we write

$$L_{1AB} = \int_B^A n_1 ds_1 + \Omega_A(t_0) - \Omega_B(t_0 - \Delta t_{AB}), \quad (5)$$

where we have made clear that the clock/relativistic terms are related to the reception time, t_0, at the LEO receiver (A) and to the transmit time a time interval $\Delta \bar{t}_{AB}$ earlier at the GPS transmitter (B). The observed phase path of the other three links in Figure 2 can be formulated similarly to (4) and (5). For the AC link, however, the refractive index only consists of a frequency dependent contribution from the ionosphere since the lowest altitude of this link is well above the neutral atmosphere. Performing a linear combination of the L_1 and L_2 phase paths on the AC link, the ionospheric contribution is eliminated to a high degree. We can therefore write the observed, but ionosphere-free phase path, L_{AC}, related to the AC link as

$$L_{AC} = |AC| + \Omega_A(t_0) - \Omega_C(t_0 - \Delta t_C), \quad (6)$$

where $|AC|$ is the geometric distance between receiver (A) and transmitter (C). Accounting for the tropospheric

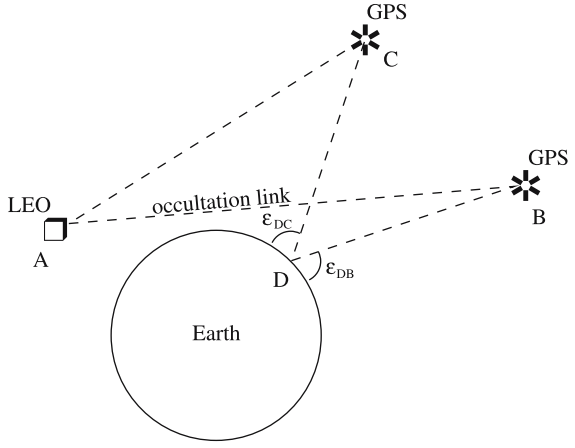

Fig. 2 Illustration of the double differencing technique. Signals from a reference GPS satellite (C) is received in LEO (A) simultaneously with the signals from the occultating GPS satellite (B). Both GPS satellites transmit signals to a ground station (D)

excess phase, τ_{DB} and τ_{DC}, experienced by links DB and DC, respectively, we can write the ionosphere-free phase path related to these links as

$$L_{\mathrm{DB}} = |\mathrm{DB}| + \tau_{\mathrm{DB}} + \Omega_{\mathrm{D}}(t_0 - \Delta t_{\mathrm{AB}} + \Delta t_{\mathrm{DB}}) - \Omega_{\mathrm{B}}(t_0 - \Delta t_{\mathrm{AB}}), \quad (7)$$

and

$$L_{\mathrm{DC}} = |\mathrm{DC}| + \tau_{\mathrm{DC}} + \Omega_{\mathrm{D}}(t_0 - \Delta t_{\mathrm{AC}} + \Delta t_{\mathrm{DC}}) - \Omega_{\mathrm{C}}(t_0 - \Delta t_{\mathrm{AC}}). \quad (8)$$

The geometric distances, |AB|, |AC|, |DB|, and |DC| are known from the orbit determination (including signal travel-time corrections). The double differencing to obtain the L_1 excess phase related to the AB link then consists of the following combination:

$$\Delta L_{1\mathrm{AB}} = (L_{1\mathrm{AB}} - |\mathrm{AB}|) - (L_{\mathrm{AC}} - |\mathrm{AC}|) - (L_{\mathrm{DB}} - |\mathrm{DB}|) + (L_{\mathrm{DC}} - |\mathrm{DC}|), \quad (9)$$

with the result that

$$\Delta L_{1\mathrm{AB}} = \int_{\mathrm{B}}^{\mathrm{A}} n_1 ds_1 - |\mathrm{AB}| + (\tau_{\mathrm{DC}} - \tau_{\mathrm{DB}}) + \Delta\Omega_{\mathrm{D}}, \quad (10)$$

where $\Delta\Omega_D = \Omega_D(t_0 - \Delta t_{AC} + \Delta t_{DC}) - \Omega_D(t_0 - \Delta t_{AB} + \Delta t_{DB})$. A similar expression can be obtained for the L_2 excess phase path (or in our case L_2*). Strictly, when differencing observations at different times, the double-differencing should be performed using the observed frequencies, not the phases. The difference is subtle and the error made can be neglected.

At the ground station $\Delta\Omega_D$ reduces to ΔQ_D, being the difference in clock error of the ground station receiver at two slightly different times. Because we assume the ground station has a very stable clock, the last term in (10) can be ignored. The tropospheric excess phases were estimated and subtracted using the mapping function given by (Foelsche and Kirchengast 2002)

$$m(\varepsilon) = \frac{\cos(\arcsin(\tilde{r}\cos\varepsilon)) - \tilde{r}\sin\varepsilon}{1 - \tilde{r}}, \quad (11)$$

where ε is the elevation angle of the satellite link, $\tilde{r} = R_{\mathrm{e}}/(R_{\mathrm{e}} + H_{\mathrm{atm}})$, R_e is the Earth's radius, and H_{atm} is an "effective height" of the atmosphere set to 15 km. The difference in excess phases was thus modeled as follows:

$$\tau_{\mathrm{DC}} - \tau_{\mathrm{DB}} = \tau_{\mathrm{D}}[m(\varepsilon_{\mathrm{DC}}) - m(\varepsilon_{\mathrm{DB}})], \quad (12)$$

where τ_D is the zenith tropospheric delay (excess phase) at the ground station and ε_{DC} and ε_{DB} are the elevation angles defined in Figure 2.

Retrieval of Atmospheric parameters

The basic equations used in the Ørsted data processing to obtain profiles of bending angle, refractivity, and so-called dry temperature, are described in (Høeg et al. 1998; Syndergaard 1998). The ionosphere-free phase path is obtained via the standard linear combination of the L_1 and L_2* phase path data. Bending angle profiles are calculated from the estimated ionosphere-free phase path using the assumption of geometrical optics treating the signal paths as rays. This assumption is justified as the Ørsted measurements usually stop above the regions of atmospheric multipath behavior where more advanced techniques are necessary, e.g., the Canonical Transform method (Gorbunov 2002) and the Full Spectrum Inversion (FSI) (Jensen et al. 2003). Due to the large uncertainty of the L_2* data, there is no advantage of performing the ionosphere correction in bending angle space as is otherwise recommended (Vorob'ev and Krasil'nikova 1994). The resulting neutral atmosphere bending angle profile is extrapolated using the MSIS-90 climatological model (Hedin 1991). For the purpose of fast computation of model bending angle profiles, the calculated refractivity from the MSIS-90 model was separated into spherical harmonics describing variations in latitude and longitude, and Chebyshev polynomials describing the vertical structure. A corresponding global model of MSIS-90 bending angle profiles was then established via the Abel integral equation relating refractivity to bending angle (Fjeldbo et al. 1971). For a given occultation, the observed bending angle profile is extrapolated using the best fitting model bending angle profile (allowing for an undetermined constant offset in the bending angle profile) within ±5° latitude and ±30° longitude. This fit is done only between 25 and 75 km where the bending angle is small. The model values are then applied to altitudes above 45 km or as low as needed until a transition point is determined where the slope of the model and the data do not differ by more than 10%. This may sometimes result in a transition level below 40 km and in about 3% of the cases even below 35 km, but in about 90% of the cases, the transition level is between 40 and 45 km. Data from the transition level and above does not directly enter the final output. However, through the Abel transform, part of the model information is contained in the refractivity also below the transition level (Marquardt et al. 2003). The relative amount of model information below the transition is reduced rapidly as the density of the atmosphere increases exponentially toward the surface. Finally, a constant shift of the bending angle profile below the transition level to match the model value at the transition level is carried out. This approach is justified only because bending angles may be biased due to the uncertainty in the Ørsted orbit determination.

Most of this bias is assumed to be a constant over the entire profile (because orbit errors are slowly varying and an orbit velocity error basically translates into a bending angle offset). Thus, the best fitting bending angle profile from the MSIS-90 model between 25 and 75 km is used to adjust the observed bending angles. We found that adjustments in the bending angle using this approach are typically between −20 and +20 μrad, but can be about 5 times larger in a few cases. Given a typical descend rate of 2 km/s of the GPS-LEO link during a setting occultation, a 20 μrad bending angle bias corresponds to a 40 mm/s velocity bias. It should be noted, however, that the bias correction procedure is complicated by the high frequency ionospheric residual left over from the single-frequency approach, as discussed earlier. By inspection of the retrieved bending angles above 45 km, we found that the standard deviation of this residual noise is about 10 μrad. Although the data is extensively smoothed above 45 km before the bias correction is performed, this residual noise limits the accuracy of the bias correction to about 10 μrad.

From the bending angle profile the refractive index is determined assuming spherical symmetry and using the Abel integral transform (Fjeldbo et al. 1971). From the refractive index, μ, we obtain the refractivity, which is defined as $N=(\mu-1)10^6$. The Abel transform suppresses high frequency noise to a certain extent (Lohmann 2005), and fractional errors in the refractivity tend to be several times smaller than the corresponding fractional errors in the bending angle (see also Syndergaard 1999; Healy 2001). At 10 km altitude, a typical bending angle is about 0.007 rad, and a 10 μrad residual ionospheric noise component corresponds to a fractional bending angle error of about 0.15%. Thus, in the troposphere, the residual ionospheric noise (which is not filtered out below 15 km) is not expected to contribute significantly to the error in the retrieved refractivity profiles. On the other hand, it can be shown that a constant bending angle error, $\Delta\alpha$, below some transition level, a_{max}, results in a refractivity error, ΔN, as a function of impact parameter, a, given by

$$\Delta N(a) = -10^6 \frac{\Delta\alpha}{\pi} \ln\left(\frac{a_{\max} - \sqrt{a_{\max}^2 - a^2}}{a}\right). \tag{13}$$

Assuming $\Delta\alpha = 10$ μrad, and using an exponential profile with typical values of the refractivity scale height (7.5 km) and the surface refractivity (300 N-units), Figure 3a shows the fractional refractivity error according to (13) as a function of altitude for different values of $a_{\max}$. The altitude was obtained as $z = a/\mu - r_e$, where $r_e = 6370$ km is the Earth's radius. Although the fractional refractivity error due to a 10 μrad bending angle bias may be quite large right below the transition level, it falls off to about 1% at 20 km almost independently of the height of the transition level, and decreases further below 20 km. However, when the refractivity is expressed as a function of pressure (as we do later in this paper) the fractional refractivity error

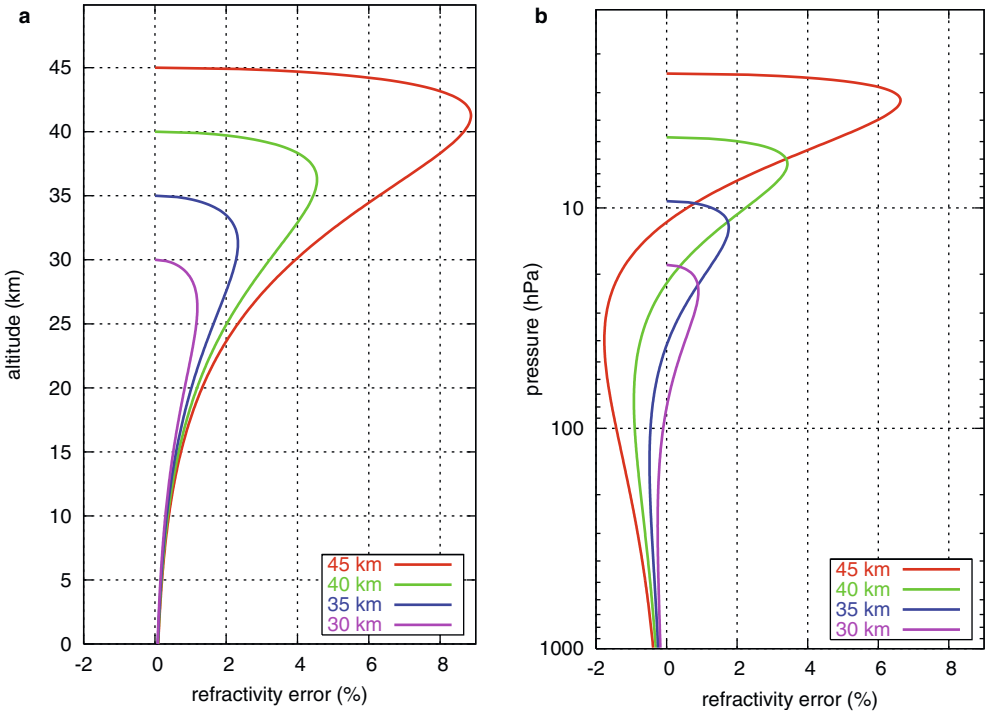

Fig. 3 Estimated refractivity errors due to a constant bending angle bias of 10 μrad below the transition level (illustrated here for four different transition levels between 30 and 45 km). (a) As a function of altitude. (b) As a function of pressure

from a 10 μrad bending angle bias becomes smaller in the upper part of the profile, but larger, and with opposite sign, in the lower part. This is shown in Figure 3b. The reason for this behavior is that the pressure is determined by integration of the refractivity (see below), and consequently the retrieved pressure will also be in error due to the bending angle bias. The net result is a maximum refractivity error of about 7% in the upper stratosphere (for the case where the transition level is at 45 km), decreasing to about −2% in the lower stratosphere, and being below −1% in the troposphere. For a negative bending angle bias of 10 μrad, the resulting refractivity errors are basically the same, but with opposite signs.

Figure 3. Estimated refractivity errors due to a constant bending angle bias of 10 μrad below the transition level (illustrated here for four different transition levels between 30 and 45 km). (a) As a function of altitude. (b) As a function of pressure.

Thus, retrieved refractivity profiles, besides being affected by (smoothed) ionosphere residual noise and a priori climatology near the transition level, may have a varying bias which only becomes insignificant in the lower troposphere. In individual profiles this bias may be the dominant error throughout the stratosphere and in the upper troposphere. For the few profiles where the transition level is in the mid stratosphere, the bias will not be very large, but instead the climatology in those cases has a larger influence at lower altitudes. Statistically, the result of the errors in Figure 3 could be both a larger standard deviation and a mean bias (if there is a mean bias in the bending angles).

The refractivity is related to the atmospheric temperature, pressure and water vapor pressure. If water vapor pressure can be neglected, refractivity is directly proportional to density, and a pressure profile can then be derived assuming the atmosphere to be in hydrostatic equilibrium. Via the ideal gas law, a temperature profile can then be obtained. This procedure has become common use even when the water vapor pressure can not be neglected (in the lowest part of the troposphere) and the resulting temperature estimate (assuming the water vapor pressure to be zero) has been termed the "dry temperature". Similarly, the pressure profile obtained via hydrostatic integration of refractivity, assuming no water vapor, can be termed "dry pressure", but should not be confused with the partial pressure of dry air. In the lower troposphere the dry temperature is generally different from the actual temperature. On the other hand, if the actual temperature profile is known from other sources, a humidity profile can be solved for (e.g. Høeg et al. 1998). Humidity profiles from Ørsted measurements have not been achieved as the profiles in most cases have terminated above heights of 5 km.

Ørsted measurements

The largest campaign carried out with the TurboRogue receiver on Ørsted lasted 20 days covering the period 3–22 February 2000. During this campaign more than 1200 occultation events were measured by the TurboRogue instrument. Refractivity and dry temperature profiles from Ørsted have been compared with NWP analysis results from the European Center for Medium-range Weather forecast (ECMWF). The ECMWF data, interpolated horizontally to the location of the occultation, are delivered as temperature and geopotential height at 16 fixed pressure levels between 1000 and 1 hPa, and specific humidity at levels up to 10 hPa. The ECMWF pressure, temperature, and humidity data were first converted to refractivity as a function of geopotential height. Dry pressure and dry temperature profiles, as defined for the occultation measurements, were then derived via hydrostatic integration assuming no water vapor. Refractivity and dry temperature, as a function of dry pressure, were finally interpolated back to the 16 fixed pressure levels. Global NWP analysis is performed every 3 hours. Thus, the maximum offset in time in reference to an occultation event is 1.5 hours.

Figure 4 shows the statistics of the comparisons between the Ørsted data (a total of 1238 profiles) and the ECMWF analyses (Ørsted minus ECMWF) for both refractivity and dry temperature. In each plot, the mean deviation is marked by the red line whereas the blue lines represents plus/minus one standard deviation. The magenta lines represents plus/minus one standard deviation of the mean, which is calculated as the standard deviation divided by the square root of the number of observations at each level. The large standard deviation of the mean at the lowest levels, indicate that only a few profiles reach these levels. At a given pressure, refractivity and dry temperature are inversely proportional to each other which explain why the dry temperature statistics is basically a reflected image of the refractivity statistics. In the following we only discuss the dry temperature results since the same features, but with opposite sign, can be found in the refractivity results (although there in terms of percent). In the height interval between 500 and 30 hPa the mean dry temperature difference from ECMWF is only about 0.5 K or less, with a standard deviation of 2 to 4 K. Above the 30 hPa level the mean difference increases rapidly, and is probably more due to a bias in the retrieved refractivity from the Ørsted data than in the ECMWF data. We suspect the bias to be a result of the residual ionosphere error, leading to imperfect bias correction of bending angles in an attempt to mitigate the velocity bias from orbit determination (cf. Figure 3b). Part of the bias may also originate from the use of the MSIS90 model to

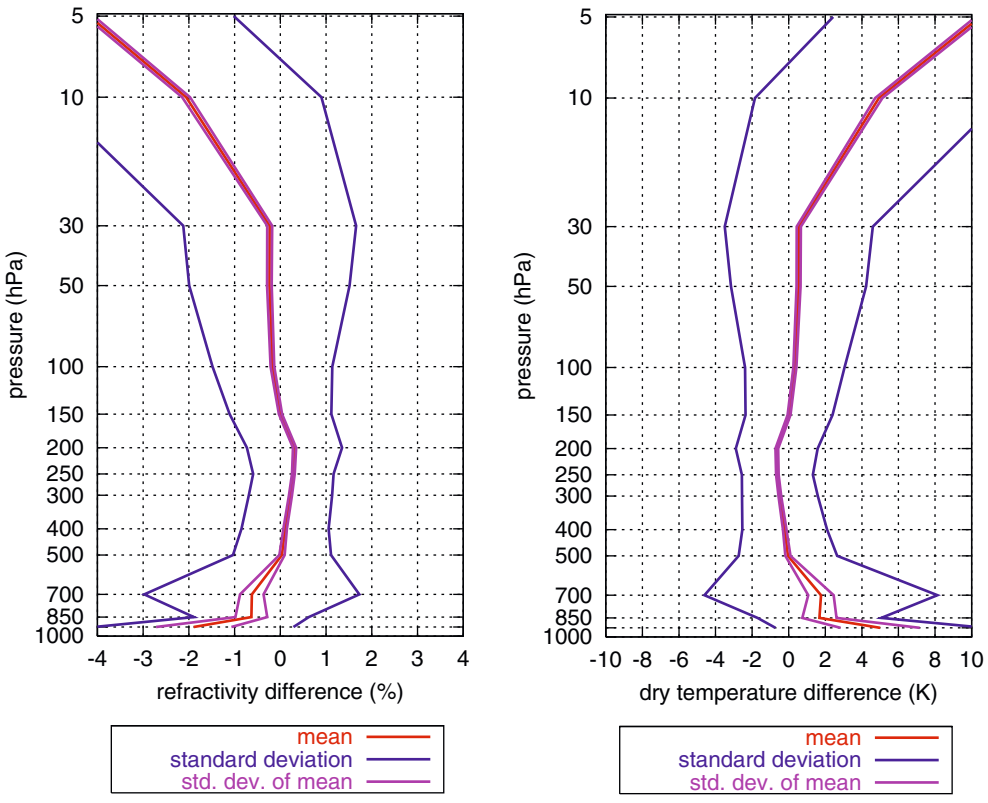

Fig. 4 Ørsted-retrieved refractivity and dry temperature profiles compared with ECWMF-derived refractivity and dry temperature profiles. Pressure values on the ordinates indicate the ECMWF levels (except one at 925 hPa) where comparisons were made

initialize the retrieval of refractivity. An increase in the mean difference (and standard deviation) is also seen below the 500 hPa level. This is thought to be due to erroneous tracking by the TurboRogue receiver using a phase-locked loop with a bandwidth of only 10 Hz. To capture the large phase accelerations associated with atmospheric multipath interference in the moist lower troposphere, open loop tracking with a bandwidth of at least 50 Hz is necessary (Sokolovskiy 2001). The positive bias in dry temperature below 500 hPa corresponds to a negative refractivity bias. Similar negative refractivity biases have been observed in GPS/MET (Rocken et al. 1997) and CHAMP data (Ao et al. 2003). The decreasing number of observations from the 400 hPa level and down is another result of the difficulties for the TurboRogue receiver onboard the Ørsted satellite in tracking the signal in the lower troposphere.

To assess the impact of geographical location and the global distribution of water vapor on the temperature statistics, we have divided the analysis into regions of "low" latitudes between 40°S and 40°N, and "high" latitudes, north of 40°N and south of 40°S (Figure 5). First of all we see a noticeably smaller standard deviation at and above the 300 hPa level at low latitudes as compared to high latitudes. This may indicate a larger general variability in the stratospheric temperature at high latitudes, not captured by either the Ørsted retrievals or the ECMWF analyses. We suspect that the Ørsted retrievals do not capture small-scale vertical variations in the upper stratosphere because the bending angles are extensively smoothed at these altitudes to reduce the large ionospheric residual error stemming from the single frequency approach. On the other hand, we see a small positive mean difference (less than 1 K) at low latitudes between 100 and 30 hPa, which do not appear at high latitudes. This suggest a cold bias in the ECMWF analyses in the lower stratosphere at low latitudes, but in the light of the possible refractivity errors due to imperfect bias correction of bending angles, as shown in Figure 3, any definite conclusions about the ECMWF analyses in this height range should not be based on the Ørsted data alone.

The statistics also show negative temperature biases of a little more than 0.5 K at about 250–300 hPa at high latitudes and at 200 hPa at low latitudes. We interpret this as a clear indication of the relatively poor resolution of the tropopause in the ECMWF analyses as compared to the relatively high vertical resolution of the Ørsted retrievals at these altitudes. This interpretation is also consistent with the fact that the tropopause generally is located at higher altitudes at low latitudes. A similar negative temperature bias around the tropopause is also observed using CHAMP radio occultation data compared against ECMWF (Steiner 2004, Wickert 2004). As

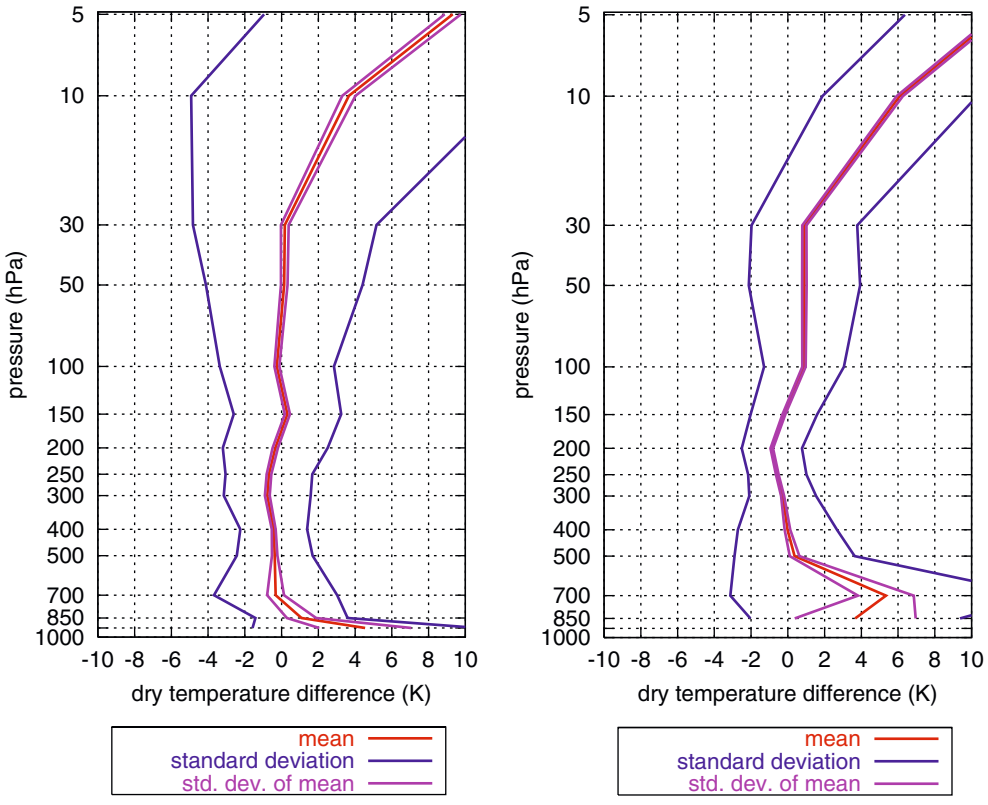

Fig. 5 Ørsted-retrieved dry temperature profiles compared with ECWMF-derived dry temperature profiles for high latitudes (larger than 40°; left panel) and low latitudes (less than 40°; right panel)

an example, Figure 6 shows a retrieval of the dry temperature profile for Ørsted occultation#08–19 on February 8, 2000. Also shown is the corresponding ECMWF temperature and ECMWF-derived dry temperature. It is clear in this example that the Ørsted retrieval captures a sharp tropopause minimum, while the tropopause minimum in the ECMWF analysis is less pronounced.

Finally the positive mean differences and the increase in standard deviations in the lowest part of the atmosphere (Figure 5) indicate that the tracking generally fails below the 500 hPa level at low latitudes, whereas at high latitudes it seems to work well down to 700 hPa. As mentioned above, erroneous tracking can be explained by increased moisture in the troposphere, and the statistical results are consistent with the fact that there is generally more tropospheric moisture at low latitudes than at high latitudes.

Discussion

With the addition of the TurboRogue GPS receiver on the Ørsted satellite, the Ørsted mission, with the primary goal to measure the Earth's magnetic field, became the second mission capable of measuring GPS radio occultations. The success of these measurements was limited by a combination of factors such as; low signal-to-noise ratio, Anti-Spoofing (AS) on at all times, interference with the attitude control system causing data gaps, and at times rotating satellite platform due to attitude control problems in the first year of the Ørsted mission. This demanded an adjustment of the processing technique to deal with the Ørsted GPS occultation data.

We have here presented the Ørsted data processing of GPS radio occultations using the single frequency method. As discussed above, the accuracy of the single frequency method is fundamentally limited by the high-frequency ionosphere residual noise, which is significantly larger than when using both frequencies (if available). However, useful retrievals can still be made and our analysis shows that the dominating error in individual profiles above 500 hPa probably is a slowly varying bias, which is at most 1% near the tropopause. The single frequency technique has also the potential to be used on other GPS occultation datasets to increase the available number of occultation retrievals. It can be used to process the GPS/MET data in periods where AS was on to obtain a larger data record for climate monitoring (de la Torre Juárez 2002), on future single frequency missions, or on mission where in a subset of the data the L_2 tracking has failed.

The comparisons with ECMWF analyses show that the Ørsted single frequency data does provide reasonably accurate retrievals of the refractivity and dry temperature in the region between 500 and 30 hPa.

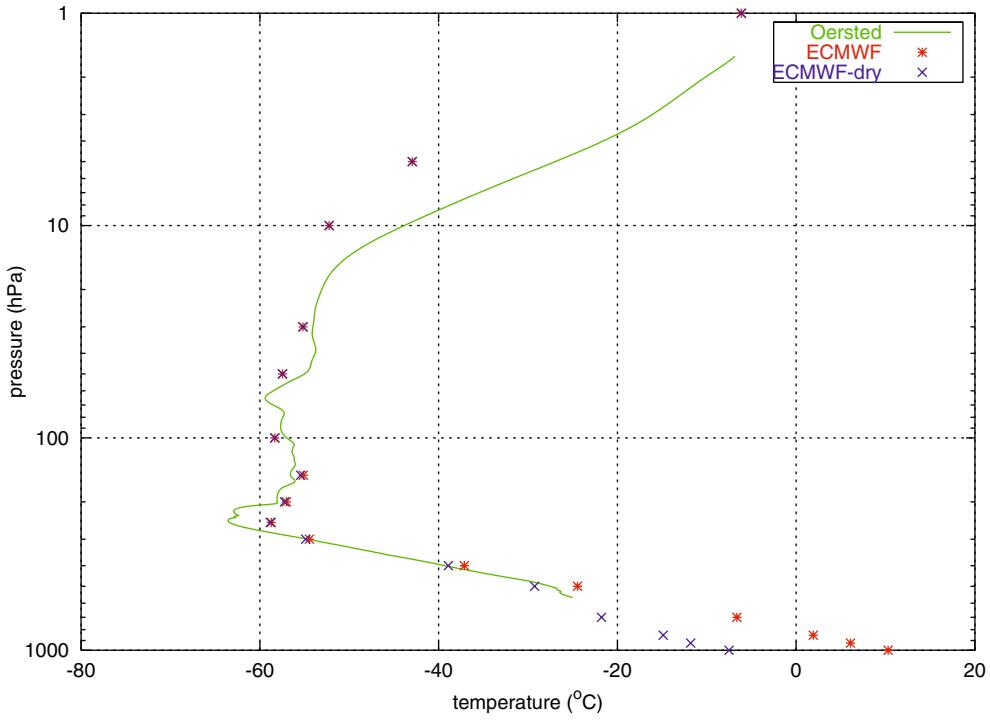

Fig. 6 Temperature profiles related to Ørsted occultation no. 00.039.17:36_ORST.08-19_26.FAIR which took place on February 8, 2000, at 17:36 UTC. The location was at 40.3°N, 70.2°E

Compared to the dual frequency results from GPS/MET (Rocken et al. 1997) and CHAMP (Wickert et al. 2003) the standard deviation on dry temperature using the single frequency retrieval is about a factor of 1.5 to 2 larger. Most of this difference, as well as a bias above 30 hPa, can be explained by the errors shown in Figure 3b.

The single frequency method can also be applied for the retrieval of electron density in the ionosphere. Electron density profiles have been obtained by the GPS/MET experiment using dual frequency total electron content (TEC) measurements (Hajj and Romans 1998; Schreiner et al. 1999). For the Ørsted data, electron density profiles have been obtained via a single frequency combination of the L_1 and C_1 data to derive the TEC (Larsen et al. 2000). Like the dual frequency combination, this single frequency combination does not require precise orbit determination, and clock errors are inherently eliminated. The single frequency combination does, however, introduce more noise in the estimation of both the TEC and the subsequently derived electron density profile. The method works well when the electron density is high and comparisons between Ørsted GPS occultations and nearby CHAMP GPS occultations show good agreements (Stauning et al. 2002).

Conclusions

Using the single frequency technique as outlined in this paper we have processed Ørsted GPS occultation measurements into atmospheric profiles of refractivity and dry temperature. The single frequency method is limited compared to having both frequencies available through the difficulty of ionosphere correction. Much more noise is introduced when using the pseudo-range measurements for ionosphere correction. We found that the residual noise probably limits the accuracy of a bias correction applied to the bending angles in an attempt to mitigate the effect of large satellite orbit errors. The impact on the accuracy of the retrieved refractivity (and similarly temperature), when expressed as a function of pressure, may be up to 7% in the upper stratosphere, but probably less than 2% in the lower stratosphere, and less than 1% in the troposphere.

The retrievals are compared to analysis data from the ECMWF. For the Ørsted GPS campaign in February 2000 we find a mean difference in dry temperature of less than 0.5 K and a standard deviation of 2–4 K between 500 to 30 hPa in height. The standard deviation is generally smaller at low latitudes than at high latitudes, indicating larger temperature variability at high latitudes not captured by either the data or the ECMWF analyses. A clear indication of the ECMWF analyses inability to adequately resolve the tropopause temperature minimum at both low and high latitudes is seen in the statistics. This is also found when using CHAMP data (Steiner 2004, Wickert 2004). The statistics also indicate a small cold-bias in the ECMWF analyses temperature at low latitudes between 100 and 30 hPa, although it is not ruled out that the Ørsted data could be biased in this

range. Detailed analysis using more data e.g. from CHAMP is needed to clearly identify if such a bias is persistent and caused by uncertainties in the ECMWF model. Other discrepancies above 30 hPa and below 500 hPa are most likely due to errors in the retrieved temperature from the Ørsted data than in the ECMWF analyses.

Now at the beginning of 2005 the Ørsted satellite has been in orbit for six years. However, since the campaign in February 2000 the TurboRogue on Ørsted has only been turned on for a limited number of short periods (few days). Recently, occultation measurements have been collected daily, but only for 1–2 orbits (three hours or less) as part of a project to study the impact of space weather on the atmosphere retrievals.

Acknowledgements We are grateful to Bjarne Amstrup, DMI, for extracting ECMWF data for all occultation events used in this work. The Ørsted Data Center at DMI provided the raw data packages down-linked from the TurboRogue receiver onboard the Ørsted satellite. This work was sponsored by the Danish Natural Science Research Council and in part by the EUMETSAT GRAS SAF project.

References

Ao CO, Meehan TK, Hajj GA, Mannucci AJ, Beyerle G (2003) Lower troposphere refractivity bias in GPS occultation retrievals. J Geophys Res 108: 4577 DOI 10.1029/2002JD003216

Ashby N (2003) Relativity in the Global Positioning System. Living Rev Relativity 6: http://www.livingreviews.org/Articles/Volume6/2003-1ashby

Escudero A, Schlesier A, Rius A, Flores A, Rubek F, Larsen GB, Syndergaard S, Høeg P (2001) Ionospheric tomography using Ørsted GPS measurements. Phys Chem Earth 25:123–126

Fjeldbo G, Kliore AJ, Eshleman VR (1971) The neutral atmosphere of Venus as studied with the Mariner V radio occultation experiments. Astron J 76:123–140

Foelsche U, Kirchengast G (2002) A simple "geometric" mapping function for the hydrostatic delay at radio frequencies and assessment of its performance. Geophys Res Lett 29:1473 DOI 10.1029/2001GL013744

Gorbunov ME (2002) Canonical transform method for processing radio occultation data in the lower troposphere. Radio Sci 37:1076 DOI 10.1029/2000RS002592

Høeg P, Larsen GB, Benzon H-H, Grove-Rasmussen J, Syndergaard S, Mortensen MD, Christensen J, Schultz K (1998) GPS atmosphere profiling methods and error assessments. Scientific Report 98-7, Danish Meteorological Institute, Copenhagen, Denmark

Hajj GA, Romans LJ (1998) Ionospheric electron density profiles obtained with the Global Positioning System: Results from the GPS/MET experiment. Radio Sci 33:175–190

Hajj GA, Kursinski ER, Romans LJ, Bertiger WI, Leroy SS (2002) A technical description of atmospheric sounding by GPS occultation. J Atmos Solar-Terr Phys 64:451–469

Healy, SB (2001) Radio occultation bending angle and impact parameter errors caused by horizontal refractive index gradients in the troposphere: A simulation study. J Geophys Res 106:11875–11889

Hedin AE (1991) Extension of the MSIS thermosphere model into the middle and lower atmosphere. J Geophys Res 96:1159–1172

Jensen AS, Lohmann MS, Benzon H-H, Nielsen AS (2003) Full Spectrum Inversion of radio occultation signals. Radio Science, Vol. 38, NO. 3: 1040 DOI 10.1029/2002RS002763

Kliore A, Cain DL, Levy GS, Eshleman VR, Fjeldbo G, Drake FD (1965) Occultation experiment: Results of the first direct measurement of Mars's atmosphere and ionosphere. Science 149:1243–1248

Larsen GB, Zhang X-J, Hoeg P, Syndergaard S, Sørensen MB, Grove-Rasmussen J, Fukao S, Igarashi K, Kawamura S (2000) Comparison of electron density profiles from Ørsted GPS occultation data and ground-based radar observations. In: Neubert T, Ultré-Guérard P (eds) Ørsted Proceedings, 3rd International Science Team meeting, 2–4 May 2000, Grasse, France

Lohmann MS (2005) Application of dynamical error estimation for statistical optimization of radio occultation bending angles. Radio Science: in press

Marquardt C, et al. (2003) Validation and data quality of CHAMP radio occultation studies. In Proceedings: First CHAMP mission results for gravity, magnetic and atmospheric studies, Springer, 384–396

Meehan TK, Srinivasan JM, Spitzmesser DJ, Dunn CE, Ten JY, Thomas JB, Munson TN, Duncan CB (1992) The TurboRogue GPS receiver. In: Proceedings of Sixths International Symposium on Satellite Positioning, 17–20 March 1992, Columbus, Ohio, pp 209–218

Montenbruck O (2003) Kinematic GPS positioning of LEO satellites using ionosphere-free single frequency measurements. Aerospace Science and Technology 7:396–405

Rocken C, Anthes R, Exner M, Hunt D, Sokolovskiy S, Ware R, Gorbunov M, Schreiner W, Feng D, Herman B, Kuo Y-H, Zou X (1997) Analysis and validation of GPS/MET data in the neutral atmosphere. J Geophys Res 102: 29849–29866

Schreiner WS, Hunt DC, Rocken C, Sokolovskiy S (1998) Precise GPS data processing for the GPS/MET radio occultation mission at UCAR. In: Proceedings of the Institute of the Navigation—Navigation 2000, Alexandria, VA, pp 103–112

Schreiner WS, Sokolovskiy SV, Rocken C, Hunt DC (1999) Analysis and validation of GPS/MET data in the ionosphere. Radio Sci 34:949–966

Shapiro II (1964) Fourth test of general relativity. Phys Rev Lett 13: 789–791

Sokolovskiy (2001) Tracking tropospheric radio occultation signals from low Earth orbit. Radio Sci 36:483–498

Spilker JJ Jr (1980) GPS signal structure and performance characteristics. Global Positioning System vol. 1, Alexandria, VA: The Institute of Navigation, pp 29–54

Stauning P, Watermann J, Larsen GB, Sørensen MB (2002) Ørsted GPS-based detection of ionospheric structures and their comparison with other ground and satellite based observations and with models, In: Stauning P (ed) OIST-4 proceedings, 4'th Oersted International Science Team conference, 23–27 Sep 2002, Copenhagen, Denmark

Steiner AK (2004) Error Analyses of Refractivity Profiles Retrieved from CHAMP Radio Occultation Data. Scientific Report 04-02. Danish Meteorological Institute, Copenhagen, Denmark

Steiner AK, Kirchengast G, Ladreiter HP (1999) Inversion, error analysis, and validation of GPS/MET occultation data. Annales Geophysicae 17:122–138

Syndergaard S (1998) Modeling the impact of the Earth's oblateness on the retrieval of temperature and pressure profiles from limb sounding. J Atmos Solar-Terr Phys 60:171–180

Syndergaard S (1999) Retrieval analysis and methodologies in atmospheric limb sounding using the GNSS radio occultation technique. Scientific Report 99-6. Danish Meteorological Institute, Copenhagen, Denmark

Thomas JB (1995) Signal-processing theory for the TurboRogue receiver. JPL Publication 95-6. Jet Propulsion Laboratory, California Institute of Technology, Pasadena, CA

de la Torre Juarez M, Hajj GA, Kursinski ER, Kuang D, Mannucci AJ, Romans LJ (2002) Single frequency processing of GPS radio occultations. Int J Remote Sens 25:3731–3744

Twomey S (1977) Introduction to the Mathematics of Inversion in Remote Sensing and Indirect Measurements. Dover Publications Inc, Mineola, New York

Vorob'ev VV, Krasil'nikova TG (1994) Estimation of the accuracy of the atmospheric refractive index recovery from Doppler shift measurements at frequencies used in the NAVSTAR system. Physics of the Atmosphere and Ocean 29:602–609

Webb FH, Zumberge JF (1997) An Introduction to GIPSY/OASIS. JPL D-11088. Jet Propulsion Laboratory, Pasadena, CA

Wickert J (2004) Comparison of vertical refractivity and temperature profiles from CHAMP with radiosonde measurements. Scientific Report 04-09. Danish Meteorological Institute, Copenhagen, Denmark

Wickert J, Schmidt T, Beyerle G, König R, Reigber C, Jakowski N (2004) The radio occultation experiment aboard CHAMP: Operational data analysis and validation of vertical atmospheric profiles. J Meteorol Soc Japan 82:381–395

Yunck TP, Lindal GF, Liu C-H (1988) The role of GPS in precise Earth observation. Position Location and Navigation Symposium 1988, 'Navigation into the 21st Century' IEEE PLANS '88, 29 Nov–2 Dec. pp. 251–258